

Evidence of antiferromagnetism in ultrathin metallic (111)-oriented LaNiO₃ films

Margaret Kane ^{1,2,*}, Purnima P. Balakrishnan ^{3,*}, Okan Köksal ⁴, Megan Holtz ⁵, Andreas Suter ⁶,
 Michael R. Fitzsimmons ^{7,8,9}, Chao-Yao Yang ¹⁰, Christoph Klewe ¹¹, Paige Quarterman ³, Timothy R. Charlton ⁷,
 Andrew A. Herzing ⁵, Zaher Salman ⁶, Thomas Prokscha ⁶, Rossitza Pentcheva ⁴,
 Alexander J. Grutter ^{3,†} and Yuri Suzuki ^{12,‡}

¹Department of Materials Science and Engineering, Stanford University, Stanford, California 94305, USA

²Geballe Laboratory for Advanced Materials, Stanford University, Stanford, California 94305, USA

³NIST Center for Neutron Research, National Institute of Standards and Technology, Gaithersburg, Maryland 20899, USA

⁴Department of Physics and Center for Nanointegration (CENIDE) Universität Duisburg-Essen, Lotharstrasse 1, 47057 Duisburg, Germany

⁵Material Measurement Laboratory, National Institute of Standards and Technology, Gaithersburg, Maryland 20899, USA

⁶PSI Center for Neutron and Muon Sciences, 5232 Villigen PSI, Switzerland

⁷Neutron Scattering Division, Oak Ridge National Laboratory, Oak Ridge, Tennessee 37831, USA

⁸Department of Physics and Astronomy, University of Tennessee, Knoxville, Tennessee 37996, USA

⁹Shull Wollan Center—A Joint Center for Neutron Sciences, Oak Ridge, Tennessee 37831, USA

¹⁰Department of Material Science and Engineering, National Yang Ming Chiao Tung University, Hsinchu 300093, Taiwan

¹¹Advanced Light Source, Lawrence Berkeley National Laboratory, Berkeley, California 94720, USA

¹²Department of Applied Physics, Stanford University, Stanford, California 94305, USA



(Received 13 May 2024; revised 15 October 2024; accepted 12 November 2024; published 11 December 2024)

Antiferromagnets with exotic spin textures promise low-power spintronic devices with extremely high operating frequencies and resistance to external perturbations. In particular, the combination of highly tunable correlated electron physics, as in complex oxides, with metallicity and antiferromagnetism is desirable but exceedingly rare. LaNiO₃, the lone example of a perovskite nickelate which is metallic across all temperatures, has long been a promising candidate, but the antiferromagnetic metallic state has remained elusive. We demonstrate the emergence of this state in ultrathin films of (111)-oriented LaNiO₃ using a combination of polarized neutron reflectometry, low-energy muon spectroscopy and anomalous Hall effect measurements, and density functional theory calculations with a Hubbard U term. Further, we find a highly strained symmetry-breaking interfacial region which may support canting of the AFM moments leading to a vanishingly small net magnetization at the film-substrate interface, providing a convenient route toward control of the Néel order. Evidence of antiferromagnetic metallic behavior in (111)LNO films highlights the role of crystal symmetry in tuning the novel quantum states in complex oxides.

DOI: [10.1103/PhysRevMaterials.8.124406](https://doi.org/10.1103/PhysRevMaterials.8.124406)

I. INTRODUCTION

Antiferromagnets (AFM) are a promising materials platform for energy-efficient spintronics. In contrast to ferromagnets (FM) and ferrimagnets (FiM), AFMs are insensitive to moderate external fields and exhibit higher characteristic frequencies while preserving nonvolatility, endurance, and low power consumption. While technological implementation has been hindered by a lack of effective schemes to control and probe AFM order, recent studies of unconventional AFMs with nontrivial topology or broken inversion symmetries have opened practical routes to Néel vector switching, and electrical readout in conductive AFMs [1–4]. Further work has successfully realized angular momentum transfer through the generation of AFM spin waves [5–8]. These advances have

brought practical AFM devices closer to reality and spurred a great deal of interest in unconventional AFMs.

Many technologically promising AFMs can be found in the family of superexchange-dominated oxide materials. Among oxides, there are many insulating AFMs but relatively few AFM metals (for example, RuO₂, CaCrO₃); as such, it is highly desirable to identify new unconventional AFM metals with tunable correlated electron physics [9–11]. Here, we report the discovery of emergent AFM in ultrathin films of (111)-oriented LaNiO₃ (LNO), identified using a combination of polarized neutron reflectivity (PNR), low-energy muon spin relaxation (LE- μ SR) spectroscopy, and magneto-transport measurements, which together provide compelling evidence for long-range magnetic order. Structural characterization of the films by scanning transmission electron microscopy (STEM) reveals a highly strained region near the interface that is associated with insulating behavior while thicker films exhibit metallicity. Evidence of AFM metallic behavior in thicker (111)LNO films highlights the role of crystal symmetry in stabilizing the rare AFM metallic state in complex oxide materials.

*These authors contributed equally to this work.

†Contact author: alexander.grutter@nist.gov

‡Contact author: ysuzuki1@stanford.edu

The phase diagram of rare earth perovskite nickelates is primarily comprised of AFM insulating, paramagnetic insulating, and paramagnetic metallic ground states [12]. A metallic AFM state remained elusive until the recent demonstration of dopant-induced conductivity in $\text{Ce}_x\text{Nd}_{1-x}\text{NiO}_3$ [13]. While the parent NdNiO_3 is a typical AFM insulator with Nd and Ni moments ordered around a $(1/4, 1/4, 1/4)$ propagation vector, $\text{Ce}_x\text{Nd}_{1-x}\text{NiO}_3$ retains both AFM order and metallicity for $0.01 \leq x \leq 0.06$. The metallic AFM state supports magnetic order exclusively on the Ni sites, suggesting that it should be possible to decouple the metal-insulator transition and rare-earth magnetism from the magnetic order on the Ni site in related systems. An ideal test case for this is LNO, the lone perovskite nickelate exhibiting paramagnetism and metallicity at all temperatures. LNO has attracted much attention for its proximity to electronic and magnetic phase transitions, e.g., the metal-insulator transition exhibited by ultrathin (001) LNO [14–24].

We demonstrate the presence of AFM ground states in ultrathin films of (111)LNO with both insulating and metallic behavior depending on thickness. In metallic films, a nonlinear, hysteretic anomalous Hall effect (AHE) emerges with temperature dependence indicating multiple complex long-range magnetic orders. Using LE- μ SR, we directly probe the magnetic fields within (111)LNO, revealing that the entire film volume is magnetically ordered below $T = 50$ K. SQUID magnetometry and PNR show no net moment in the film within the accuracy of the measurement, consistent with AFM order. However, magnetotransport measurements and density functional theory calculations with a Hubbard U term suggest a trace net magnetization may emerge near the (111)LNO/LaAlO₃ (LAO) interface. These results indicate that distortions induced by (111) epitaxy stabilize AFM in the correlated metal LNO, highlighting a new approach to stabilizing novel AFM states in complex oxides.

II. RESULTS

Longitudinal magnetoresistance (MR), angle-dependent magnetoresistance (AMR), and AHE measurements have previously provided the only evidence of long-range magnetic order in (111)LNO [25–27]. Although AHE signals are usually associated with FMs or FiMs, the reformulation of the intrinsic mechanism of the AHE in FMs in terms of the Berry curvature in momentum space has led to the prediction and observation of large AHEs in noncollinear AFMs [28,29].

Figure 1 shows the temperature-dependent magnetotransport of a representative 10 u.c. (111)LNO film, where we define “unit cell” as a single LNO plane along the [111] direction i.e., ≈ 2.23 Å. As reported previously and shown in the Supplemental Material, all thicknesses measured in this study are above the metal-insulator transition observed in (111)LNO and therefore exhibit metallic conduction [26,30]. The increasing magnitude of the AHE [Fig. 1(a)] and the development of negative, hysteretic MR [Fig. 1(b)] both indicate magnetic order. The saturated AHE signal normalized by the average total $\overline{R_{xy}}$ [Fig. 1(c)] can be fit to estimate a magnetic ordering temperature of 54 K, in agreement with previous work. Notably, the nonlinear AHE contribution is nonhysteretic above 30 K, but upon cooling below 30 K, hys-

teresis emerges and the AHE coercivity H_C increases rapidly, exceeding 4 T at 2 K. The hysteresis in the longitudinal MR (ΔR_{xx}^{hyst}), defined as the maximum difference between the ascending and descending MR curves, follows a similar trend. Thus, the temperature dependences of the AHE coercivity and MR contrast starkly with that of the saturated AHE magnitude and indicate two distinct ordering temperatures.

To understand these two transitions, we investigated the temperature-dependent AMR, shown in Fig. 1(d). The AMR lineshape evolves significantly between 50 K and 20 K, exhibiting twofold in-plane symmetry at 50 K and acquiring additional periodicities upon cooling. Surprisingly, these additional AMR periodicities largely disappear at 2 K. Low-temperature AMR confirms an increase in magnetic anisotropy, with hysteresis between the ascending and descending AMR branches of in-plane angle ϕ present at 2 K even in a $H = 9$ T applied magnetic field [Fig. 1(e)]. The fast Fourier transform (FFT) of the AMR data reveals three primary symmetry contributions in the AMR, with temperature dependences shown in Fig. 1(f). The film is twofold dominant at 50 K, but cooling to 30 K yields increased fourfold and sixfold symmetry contributions while the twofold contribution remains constant. At 30 K, the twofold and fourfold FFT contributions are of the same magnitude, while cooling below 30 K results in a rapid increase in the twofold Fourier component, while fourfold and sixfold symmetries remain constant to 10 K and then sharply decrease. At 2 K, the AMR is again overwhelmingly dominated by twofold symmetry. Similar to the AHE, the AMR supports a picture in which magnetic order is stabilized between 50 K and 60 K, but at 30 K undergoes a transition that modifies the anisotropy.

Recalling that previous x-ray diffraction studies have indicated significant structural reconstructions near the (111)LNO/LAO interface [26], we probed the local structure and strain state of the films using STEM and nanobeam electron diffraction (4D-STEM) as shown in Fig. 2. Full characterization and strain analysis can be found in the Supplemental Material [30]. At the (111)LNO/LAO interface, the out-of-plane lattice parameter is approximately 0.1 Å larger than the rest of the LNO film. This expansion is consistent with our previously published synchrotron XRD studies [26]. In comparison, the in-plane lattice parameter and other strain components (see Supplemental Materials (SM) Ref. [30]) show no significant variation at the interface or in the bulk of the film, indicating a coherently strained film without rotational distortions.

These interfacial reconstructions imply that understanding the long-range magnetic order requires spatially resolved, high-sensitivity magnetic characterization. Our efforts to detect a net magnetization through bulk magnetometry and element-specific x-ray magnetic circular dichroism (XMCD) yield signals below the noise floors of these techniques. We therefore turn to polarized neutron reflectometry (PNR), which provides a detailed chemical and magnetic depth profile of the film and can readily detect magnetizations as low as 2 kA/m. Details of the measurement technique and fitting analysis can be found in the Methods section and SM. PNR measurements were performed on a 6 nm (26 u.c.) sample with a cap of 35 nm of sputtered AuPd. The 6 nm thickness was chosen to maximize any magnetic signal while still

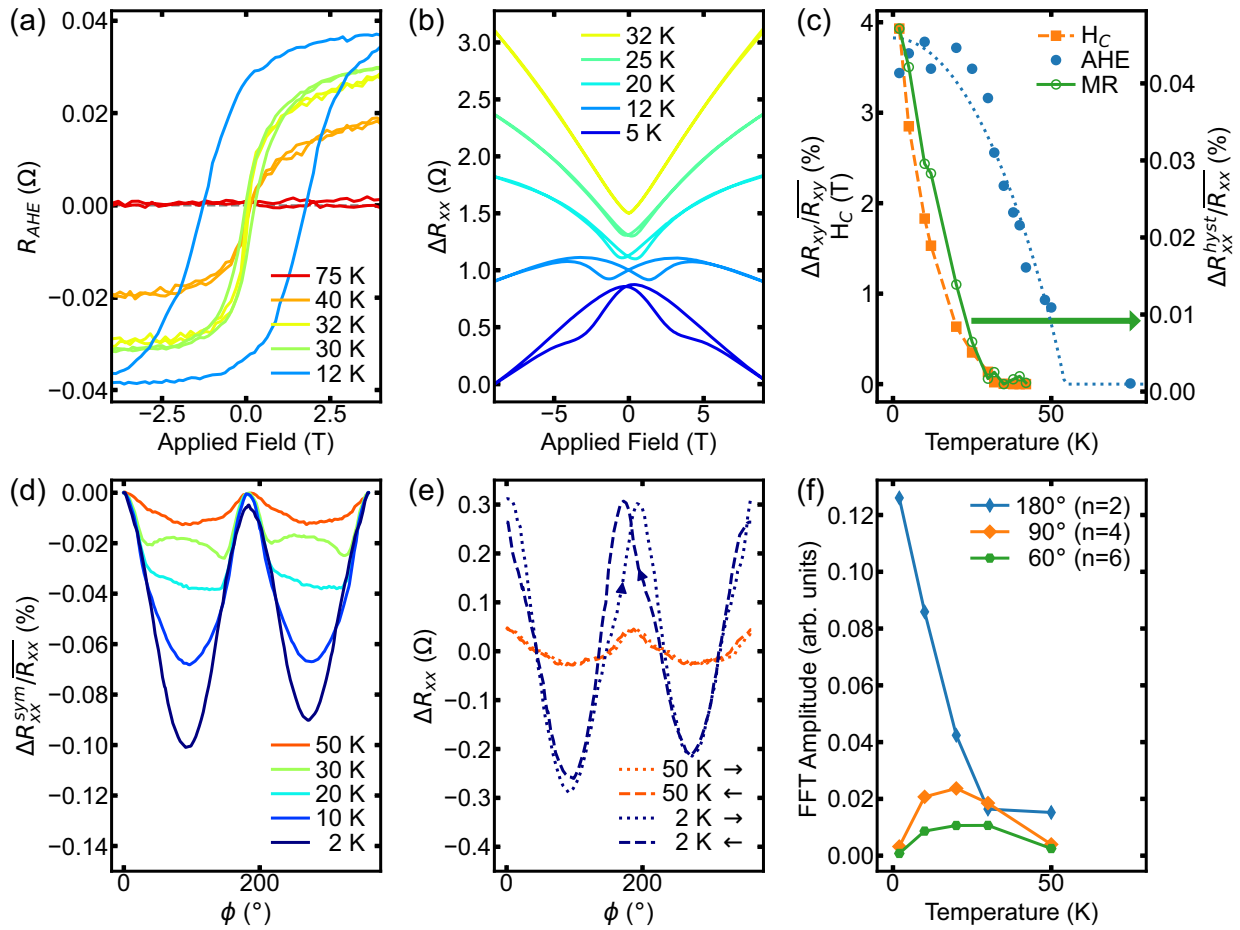


FIG. 1. (a) Temperature-dependent AHE of a 10-unit cell (111)LNO film between 2 K and 75 K. (b) Temperature-dependent longitudinal magnetoresistance of the same film. Curves offset for visibility. (c) Comparison of the saturated AHE, AHE coercivity, and longitudinal magnetoresistance hysteresis vs. temperature. The dashed line is a Brillouin function fit to the saturated AHE values suggesting an ordering temperature of ~ 50 K. (d) Temperature-dependent AMR normalized by the average longitudinal resistance as a function of temperature. Here, the ascending and descending branches of the in-plane angle ϕ have been averaged. (e) AMR at 2 K and 50 K showing ascending and descending branches of the in-plane angle ϕ . The average longitudinal resistance has been subtracted at both temperatures. (f) Temperature dependence of the Fourier components corresponding to 180° (twofold), 90° (fourfold), and 60° (sixfold) rotational symmetries.

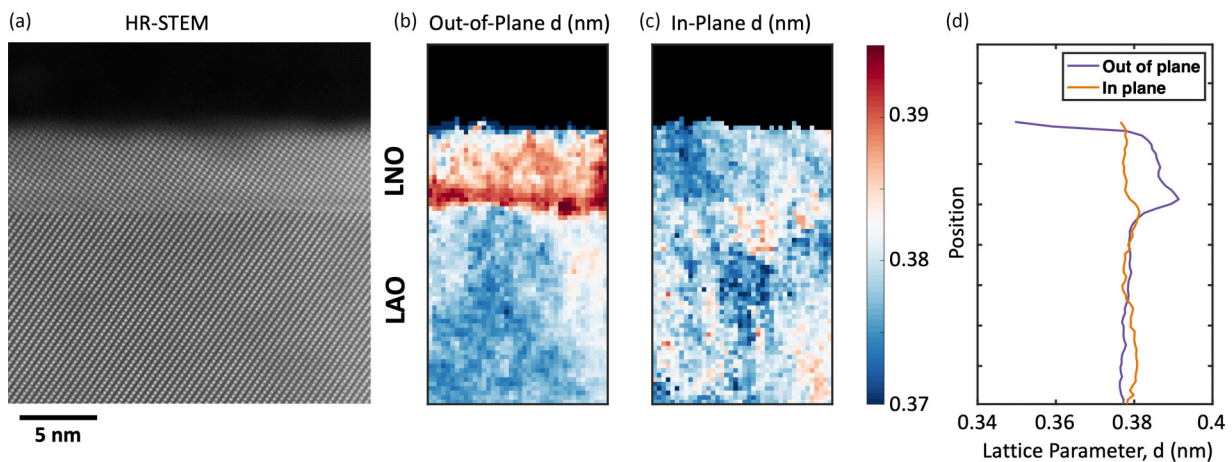


FIG. 2. (a) High-resolution STEM image of (111)LNO/LAO projected along the $[1\bar{1}0]$ direction. Lattice parameter (d_{100} equivalent) measurements from 4d STEM in the (b) $[111]$ out-of-plane direction, (c) $[110]$ in-plane direction, with (d) the corresponding line profiles. Increased out-of-plane lattice parameter is seen at the film-substrate interface, while the in-plane lattice parameter shows coherent strain. The d_{100} equivalent notation here refers to the associated pseudocubic $[100]$ -type direction after scaling to the diffraction planes actually measured.

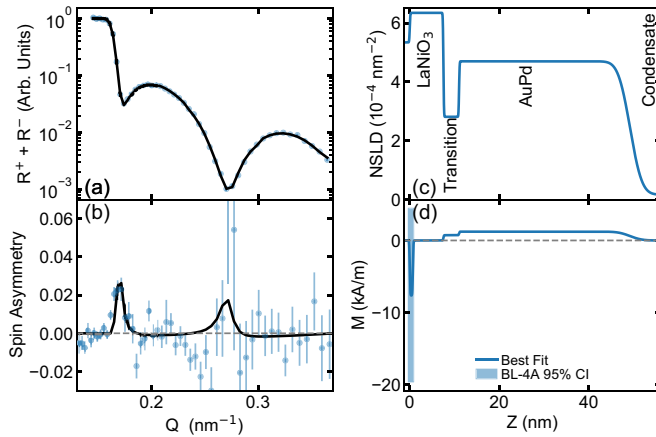


FIG. 3. (a) Sum of spin-up (R^+) and spin-down (R^-) neutron reflectivities from a (111)LNO (6 nm) / AuPd (35 nm) film on LAO, alongside a theoretical fit. (b) Spin asymmetry of the reflectivity data shown, alongside a theoretical fit. (c) Nuclear and (d) magnetic scattering length density profiles associated with the fits shown. The shaded region represents the 95% confidence interval range of the LNO magnetization obtained using the interface model. Error bars represent ± 1 standard deviation.

preserving a measurable AHE (Fig. S1). The capping layer increased the number of oscillations in the observable Q range, improving sensitivity. Long count times yielded such high magnetic field sensitivity that even the weak paramagnetism of the $\text{Au}_{0.6}\text{Pd}_{0.4}$ capping layer must be accounted for; we find a net magnetization in the cap of (1.31 ± 0.024) kA/m, as expected for $H = 4.8$ T [31–33].

We considered two candidate models of the depth profile. The first (Fig. 3) confined any net magnetization to the first few LNO unit cells (interfacial magnetism) while the second (Fig. S2) allowed for magnetism throughout the entire LNO layer (bulk magnetism) [30]. Both models were optimized when the magnetization of the LNO layer was negative and extremely small, with best-fit values corresponding to (-0.047 ± 0.038) μ_B/Ni for the interfacial model and (-0.007 ± 0.004) μ_B/Ni for the bulk model. The upper limits (95% confidence) on the magnetization were 0.03 μ_B/Ni and 0.006 μ_B/Ni for the interfacial and bulk magnetism models, respectively.

PNR was also performed on a thick 38 nm (175 u.c.) sample with no cap yielding essentially the same result as the previous measurement, with a 95% confidence upper bound of 0.02 μ_B/Ni for the interfacial magnetism model (Fig. S5) and 0.008 μ_B/Ni for the bulk magnetism model (Fig. S6) [30]. The PNR measurements place extremely tight upper limits on the net magnetization of both samples, in agreement with null results from both SQUID magnetometry and element-specific XMCD. We therefore conclude that any net magnetization must be vanishingly small, consistent with AFM or nearly compensated FiM.

To further characterize the magnetic order, we performed LE- μ SR measurements—which are sensitive to magnetic order even without a net magnetization—on 6 nm thick (111)LNO/LAO films. Spin-polarized muons (μ^+) were implanted into the sample, where they precess about an ex-

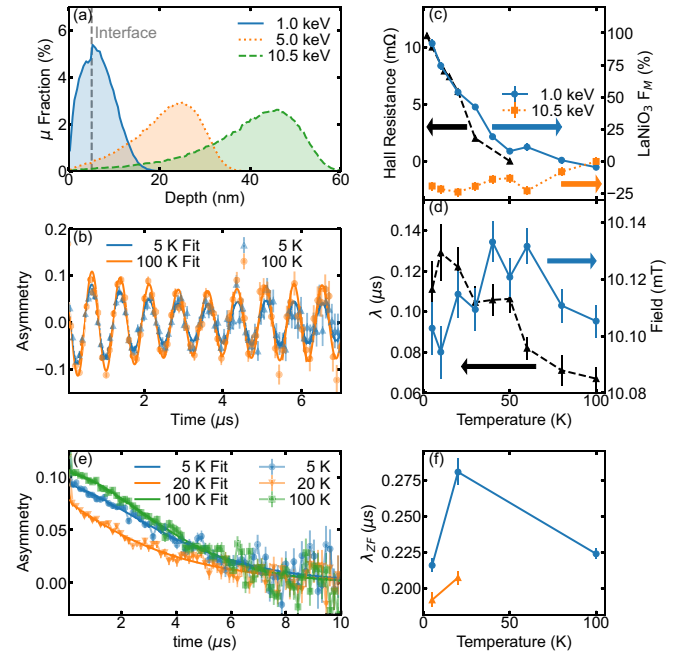


FIG. 4. (a) Simulated stopping profiles show 31% of 1 keV muons stop within the (111)LNO film. (b) Asymmetry spectra $A(t, T)$ for two temperatures. (c) Temperature dependence of Hall resistance (black triangles) and magnetic volume fraction $F_M(T)$ within the (111)LNO (blue circles) and within the LAO substrate (orange squares). (d) Depolarization rate λ (black triangles) and internal measured field (blue circles) of the (111)LNO film (1.0 keV). (e) Temperature-dependent zero-field LE- μ SR measurements performed at an implantation energy of 1 keV, alongside fits to the data. (f) Fitted zero-field asymmetry values for the slow exponential decay function vs. temperature.

ternally applied magnetic field and decay, emitting positrons preferentially along the spin direction. The directional asymmetry of positrons detected at time t and temperature T , $A(t, T)$, can be expressed as

$$A(t, T) = A_0(T)e^{-\lambda(T)t} \cos(\omega_L t), \quad (1)$$

where λ is the depolarization rate and ω_L is the Larmor precession frequency in the applied magnetic field. To implant precisely at the surface of an ultrathin film, slow-moving μ^+ s must be used, limiting the inherent time resolution of the measurement. While ω_L is low enough for asymmetry oscillations to be detected in nonmagnetic samples, muons that stop in a magnetically ordered region of the film experience a broad field distribution and depolarize much faster than the measurement time. These μ^+ s do not contribute to the measured asymmetry, decreasing A_0 . The magnetically ordered volume fraction, F_M , can then be determined by comparing the asymmetry ratio above and below the ordering temperature and normalizing for the fraction of μ^+ s stopping in the magnetic layer.

Measurements were performed using μ^+ implantation energies of 1 keV and 10.5 keV while cooling from 100 K to 5 K in a 10 mT applied magnetic field. As shown in the simulated implantation profiles of Fig. 4(a), a large fraction of 1 keV μ^+ s stop within the LNO, while 10.5 keV μ^+ s are

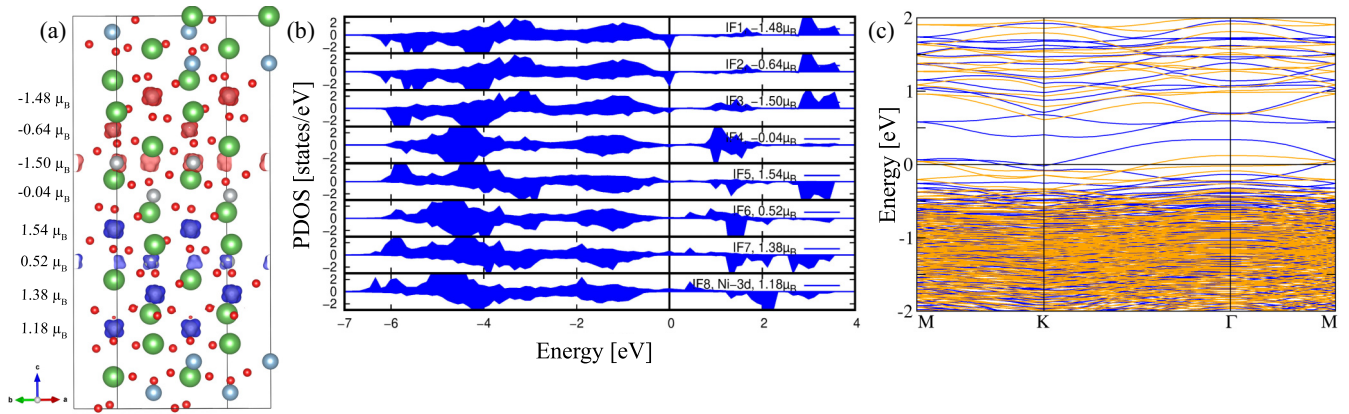


FIG. 5. (a) Side view of the isosurface of the spin densities where blue (red) show the majority (minority) contributions for the (LaNiO₃)₈/(LaAlO₃)₄(111) SL. The corresponding layer-resolved PDOS is displayed in (b). (c) Spin-resolved band structures, blue/orange denote majority/minority bands.

implanted almost exclusively into the LAO substrate. Figure 4(b) shows $A(t, T)$ at both 5 K and 100 K for 1 keV μ^+ s. As the temperature is lowered, the oscillation decreases in magnitude and decays more quickly, indicating higher magnetic volume fraction and μ^+ depolarization rate, respectively.

Figure 4(c) shows a correlation between $F_M(T)$ and the saturated AHE resistance in 6 nm (111)LNO. F_M increases gradually below 50 K, and at the lowest temperature of 5 K, F_M exceeds 90% and is still increasing, indicating that nearly the entire 6 nm LNO film orders magnetically at a low temperature. As expected, there is no notable temperature dependence in the substrate. The depolarization rate experienced by 1 keV μ^+ s increases sharply below 60 K, indicating a magnetic transition, but does not return to the prior value as expected. Instead, λ plateaus briefly before increasing again at 30 K. These two transitions match the AHE onset and hysteresis onset temperatures shown in Fig. 1(b). Alternatively, this could be interpreted as a broad percolative transition, although the distinct temperature regions previously identified make this explanation less plausible. Further, the effective field within the disordered regions of LNO [Fig. 4(d)] peaks at approximately 50 K, indicating a transitory increase in magnetic susceptibility.

To confirm the transverse-field LE- μ SR results, we also performed measurements in zero applied magnetic field as shown in Fig. 4(e). Zero-field (ZF) LE- μ SR measurements require significantly longer count times than transverse field measurements, but allow more definitive detection of magnetic transitions through precise determination of the muon depolarization rate. In this case, we fit our asymmetry, after a rapid initial decay, to a stretched exponential with the form

$$A(t, T) = A_0(T) \left(e^{-(\lambda_{ZF}(T)t)^\beta} \right). \quad (2)$$

The interpretation of zero-field LE- μ SR is complex and subtle, especially in the present case where a large fraction of the implanted μ^+ s are either reflected from the surface or implanted into the nonmagnetic LaAlO₃ substrate. Nevertheless, it is expected that a magnetic transition will cause the fitted zero-field depolarization rate (λ_{ZF}) to peak on cooling through a magnetic transition before then falling as the temperature

is further lowered. This is precisely the behavior observed in Fig. 4(e), where λ_{ZF} peaks at 20 K for an implantation energy of 1 keV. At 5 keV, which mostly probes the LaAlO₃, there is no statistically significant variation in λ_{ZF} from 5 K to 20 K. The ZF LE- μ SR therefore indicates that the LaNiO₃ films are in the middle of a magnetic transition that has largely been completed by 5 K. This is in agreement with the transverse field results that suggest the entire film is magnetically ordered by 5 K.

Our results indicate that ultrathin (111)LNO/LAO films gradually evolve from magnetic disorder above 55 K to a fully magnetically ordered state at 5 K, with at least two distinct temperature regimes i.e., 0 K to 30 K and 30 K to 50 K. The low-temperature state is marked by twofold symmetry within the (111) plane and large coercivity, while the higher-temperature state is identified by a mix of twofold, fourfold, and sixfold symmetry. Although the fully ordered state exhibits a vanishingly small net magnetization, the observation of hysteresis in the MR, AMR, and AHE suggests either a minority volume fraction exhibiting FM/FiM order or a weakly canted AFM. In either case, we suspect that the two observed temperature regions indicate either separate AFM and FM/FiM ordering temperatures or an AFM to canted AFM transition.

The highly strained region observed at the interface is an excellent candidate for hosting magnetic states different from the rest of the LNO film, and we posit that this modified interface provides a net magnetization that evades detection due to spatial localization and small magnitude. To identify potential interfacial electronic and magnetic ground states, we performed density functional theory calculations with a Hubbard U term (DFT+ U) of (LaNiO₃)₈/(LaAlO₃)₄(111) superlattices where the lateral lattice parameter was fixed to the one of LaAlO₃ to simulate epitaxial growth. Besides the FM configuration, we examined three AFM configurations between layers of the 8 u.c. LNO: AFM1 $\uparrow, \uparrow, \uparrow, \uparrow, \downarrow, \downarrow, \downarrow, \downarrow$, AFM2 $\uparrow, \uparrow, \downarrow, \downarrow, \uparrow, \uparrow, \downarrow, \downarrow$, and AFM3 $\uparrow, \downarrow, \uparrow, \downarrow, \uparrow, \downarrow, \uparrow, \downarrow$ where \uparrow / \downarrow denote the relative orientation of magnetic moments (see SM).

The most favorable configuration corresponds to the AFM1 system with two antialigned FM blocks of 4 ML each with $P1$

symmetry. Both the spin-density and the layer-resolved projected density of states (PDOS) [see Figs. 5(a) and 5(b)] show a tendency toward a layerwise disproportion at the Ni sites with values ranging from $-1.48\mu_B$ (IF1) to nearly quenched in IF4 ($-0.04\mu_B$), resulting in a ferrimagnetic state (FiM) with a nearly quenched magnetization and a net magnetic moment of $0.12\mu_B$ per Ni site. This state is energetically more stable by 0.5 eV, 0.73 eV, and 1.08 eV than the FM, AFM2 and AFM3 configurations (with alternating orientation of magnetic moments), respectively. For the AFM1 arrangement, the spin-projected band structure [Fig. 5(c)] shows a set of two dispersive majority and two minority bands crossing the Fermi level which are mainly contributed from the interface layers (IF1/IF2 and IF7/IF8) and lead to a metallic state. In contrast, band gaps of 0.34 eV and 0.27 eV open for the AFM2 and AFM3 cases, while a semimetallic band structure emerges in the FM case. Hence, DFT + U calculations confirm that a region of (111)LNO constrained through epitaxy is an excellent candidate to stabilize the experimentally observed AFM metallic state with a slight parasitic net magnetization. These calculations consequently explain both the appearance of AHE hysteresis and the vanishingly small net moment.

III. DISCUSSION AND CONCLUSIONS

(111)LNO films thus exhibit a fully magnetically ordered ground state with vanishingly small net magnetization and evidence of multiple magnetic transitions, indicating a complex magnetic order with the bulk of the (111)LNO films being both AFM and metallic below approximately 50 K. Previously, Guo *et al.* presented neutron and susceptibility data supporting AFM ordering below 157 K in LNO single crystals [34]. This work claimed high-quality, metallic LNO single crystals, essentially free of Ni^{2+} impurities, with G-type AFM and metallicity. However, extensive follow-up experiments and theoretical studies have noted that these observations are better explained by the presence of ordered oxygen vacancies [35–39]. Specifically, AFM with similar transport properties and Néel temperatures has also been observed in oxygen-deficient LaNiO_3 , as well as in $\text{LaNiO}_{2.5}$ [35,36]. We note in particular the challenge of characterizing the Ni valence in bulk crystal samples using x-ray absorption measurements which probe only a tiny fraction of the crystal volume near the surface, as in Ref. [34]. Without a direct probe of the AFM-ordered volume fraction or a volume-averaged Ni-valence, excluding oxygen-deficient ordered vacancy phases is very difficult.

On the other hand, total-electron yield x-ray absorption measurements of our ultrathin films probe the entirety of the film, so that there is nowhere for an oxygen-deficient phase to hide. Further, the LE- μ SR results show magnetic order throughout the entire film, again leaving no portion of the film in which oxygen-deficient AFM phases may evade detection. Previously reported (Ref. [26]) and new (Fig. S10) x-ray absorption measurements demonstrate a dominant Ni^{3+} valence in the bulk of the 6 nm thick films [30]. Further, no ordered oxygen defect structures were observed in our STEM results, nor in previous diffraction measurements [26]. Lastly, we note

that the 50 K to 60 K transition temperature reported here is very far from the approximately 150 K transition reported in bulk crystals. For all of these reasons, we may exclude the possibility of domains of $\text{LaNiO}_{2.5}$ surrounded by metallic LNO. Rather, the AFM reported here appears to be an intrinsic property of the unique (111)-oriented strain state induced in our LNO films.

The phase diagrams of other bulk rare earth nickelates are comprised of AFM insulating, paramagnetic insulating, and nonmagnetic metallic regions. In rare earth nickelate thin films other than LNO, AFM has been observed but with a suppressed Néel temperature compared to their bulk counterparts; examples include EuNiO_3 [40], SmNiO_3 [41], NdNiO_3 [42], and PrNiO_3 [43]. Furthermore, AFM ordering induced by charge transfer has been reported in multilayers of LNO [44–49]. The reported (1/4 1/4 1/4) AFM order corresponds to a fourfold rotational stacking of FM layers of LNO in the (111) orientation, and such helical order can explain the periodic modulation of the coupling through LNO between FM manganite layers in (111)-oriented superlattices [44,49]. In these cases, the LNO remains insulating. The lone example of a metallic AFM nickelate film has been achieved through doping and exists in a narrow compositional band [13]. In contrast, the (111)LNO AFM transition seen here appears to be a true case of metallic AFM without doping or rare-earth magnetism.

Previous reports examining magnetism on (111)LNO/LAO have indicated the stabilization of ferromagnetism [25]; this appears not to be the case. Rather, we come to the unexpected determination that the majority of the film is in a metallic AFM-ordered state, albeit with some indications of a weak magnetization in a minority of the film volume. LE- μ SR and PNR measurements show the stabilization of long-range AFM order below 50 K, while AHE and magnetotransport measurements are consistent with an AFM metallic state below 50 K, with hysteresis emerging below 30 K. The thinnest LNO films exhibit insulating behavior while metallic behavior emerges in thicker LNO films. Local structure as determined by 4DSTEM shows a highly strained (111)LNO layer at the interface, while DFT + U calculations identify this interface as a prime candidate for hosting a modified metallic AFM state with a small associated net moment. Specifically, we speculate that this layer likely breaks symmetry in a way that yields a vanishingly small parasitic net magnetization on the parent AFM phase for the one to two monolayers of LNO closest to the substrate interface. Lastly, we note that there have been previous unexplained reports of anomalous thermopower and magnetic susceptibility near approximately 50 K, which have appeared intermittently in the study of both films and bulk LNO [50,51]. It is possible that the hidden order suggested by these works may correspond to the magnetic ground state achieved in our (111)LNO/LAO. The existence of these multiple potential AFM states can explain the observed order and hysteresis, while also supporting a vanishingly small net magnetization. Evidence of AFM metallic behavior in (111)LNO films highlights the role of crystal symmetry in revealing and tuning the rare AFM metallic state in complex oxide materials via epitaxial strain, expanding the materials phase space that can be exploited in future oxide electronic applications.

IV. METHODS

A. Synthesis

(111)-oriented LaNiO_3 thin films were grown using pulsed laser deposition on LaAlO_3 substrates at $T = 780^\circ\text{C}$ and $P_{\text{O}_2} = 20$ mTorr (2.7 Pa) with a 248-nm KrF laser operating at a fluence of 0.8 J/cm^2 . Films ranged in thickness from 2 nm to 38 nm. These thin films were grown on 0.5 mm thick LaAlO_3 (111) single-crystal substrates. For our (111)-oriented films, one unit cell is defined as the distance between (111) planes or $d_{111} = a_{\text{LNO}}/\sqrt{3} = 2.23 \text{ \AA}$ where a_{LNO} is the pseudocubic lattice parameter of LaNiO_3 . To achieve smooth films, we used interval pulsed laser deposition, where 1 unit cell worth of material is deposited quickly (10 Hz) and the deposition is paused until the *in situ* reflective high energy electron diffraction (RHEED) signal intensity recovers and stabilizes. Thin film surface morphology was characterized with atomic force microscopy (AFM) and showed a low RMS roughness (0.064 nm to 0.285 nm). Averaged structure and film thickness were confirmed by x-ray diffraction (XRD) and x-ray reflectivity (XRR). AuPd capping of the PNR sample shown in the main text was performed *ex situ* after growth in a room-temperature chamber in order to avoid modifications to the strain state of the LNO film.

B. Transport Measurements

Magnetotransport measurements were performed using a Quantum Design Physical Property Measurement System. For magnetoresistance and Hall measurements, films were patterned into a Hall bar structure using photolithography and Ar ion milling. Contact pads were deposited via sputtering using an $\text{Au}_{0.6}\text{Pd}_{0.4}$ target. Hall bars of two different in-plane orientations—with current along the $[1\bar{1}0]$ and $[\bar{1}12]$ directions—were compared, with no observed difference in either magnetoresistance or Hall effect for a field along the out-of-plane $[111]$ direction. Due to a slight misalignment of contacts, the R_{xy} measurement contains some contribution from R_{xx} and a quadratic background contribution due to the magnetoresistance was subtracted. A linear ordinary Hall effect signal was then subtracted to extract the anomalous Hall contribution. The AHE measurements as shown in Fig. 1(c) were normalized by the average presymmetrized values of R_{xy} for each measurement.

Anisotropic magnetoresistance (AMR) measurements were performed using a horizontal sample rotator insert to vary the field direction within the film plane. Here, $\phi = 0$ is defined as a field along the current direction of $[1\bar{1}0]$. Scans were performed for both increasing and decreasing ϕ , as shown in Fig. 2(b) of the main text. This AMR signal was then symmetrized by averaging the ascending and descending branches to remove hysteresis, as shown in Fig. 2(a), prior to frequency analysis. All samples were field cooled in an $H = 9 \text{ T}$ field.

C. Polarized Neutron Reflectivity

Polarized neutron reflectometry (PNR) measurements were taken at the Polarized Beam Reflectometer (PBR) and CHRNS Chromatic Analysis Neutron Diffractometer or Reflectometer (CANDOR) instruments at the NIST Center for

Neutron Research and the Magnetism Reflectometer on beamline BL4-A at the Spallation Neutron Source (SNS) at Oak Ridge National Laboratory. On BL4-A, samples were cooled to 10 K in an applied field of 4.8 T in-plane in the $[1\bar{1}0]$ direction. Incident and scattered neutrons were polarized either spin-up or spin-down with respect to the applied magnetic field. Due to the large applied field, the difference in trajectories between spin-up and spin-down neutrons allows us to determine the polarization of scattered neutrons using the 2D detector rather than a polarization analyzer.

The specular reflectivity of spin-polarized neutrons is dependent on the depth profile of the sample magnetization parallel to the applied field, as well as the depth profile of the nuclear composition. Subtracting and normalizing the two non-spin-flip reflectivities, R^{++} and R^{--} , yields the spin asymmetry (SA), which is sensitive to the magnetization parallel to the applied field. Fitting for PNR measurements was done using Refl1D software package [52] to simulate reflectivity from a slab model. Due to the small magnetic signal, an alternative approach to polarized neutron data reduction and fitting was performed to reduce the uncertainty due to experimentally measured instrumental corrections. Rather than fitting the individual polarization cross sections ($R^{++}(Q)$ and $R^{--}(Q)$) simultaneously, a change of basis was performed on the simulated curves in order to fit spin asymmetry and average reflectivity directly. Spin asymmetry ($SA = \frac{R^{++} - R^{--}}{R^{++} + R^{--}}$) was calculated directly for each wavelength and detector angle, then combined into constant-wavelength bins. This analysis avoids the introduction of unnecessary statistical and experimental errors in normalizing by the measured incident wavelength spectrum. The average reflectivity $\bar{R} = \frac{R^{++} + R^{--}}{2}$ was calculated by exploiting the position-sensitivity of the neutron detector to combine counts into constant-Q bins. These two quantities $SA(Q(\lambda, \theta))$ and $\bar{R}(Q(\lambda, \theta))$ were then fit simultaneously using χ^2 minimization.

Additional PNR measurements were performed at both the PBR and the (CANDOR) beamlines at the NIST Center for Neutron Research. Measurements at the PBR, taken at 6 K under 2.5 T in-plane applied field, used a 4.75 \AA monochromated and polarized incident beam with polarization analysis. Measurements at CANDOR, taken at 30 K under 0.7 T in-plane applied field, used a polarized incident beam of wavelengths in the range of 4 \AA to 6 \AA . PBR and CANDOR data were reduced using the reductus software package [53]. These data were refined simultaneously with the data taken on BL-4A, using identical structures—aside from any surface adsorbates which can vary depending on sample handling and cooling—to obtain strict bounds on the magnetization profile.

D. Low-Energy Muon Spin Relaxation

Low-energy muon spin relaxation measurements were performed at the Low-Energy Muon (LEM) beamline at the Swiss Muon Source ($S\mu S$), Paul Scherrer Institute, Switzerland [54,55]. Measurements were taken on a mosaic of four identical 5 mm \times 10 mm samples between 5 K and 100 K with an applied field of 10 mT out-of-plane. The samples were cooled in a helium-flow cryostat (CryoVac, Konti). Muon implantation energy was varied between 1 keV and 10.5 keV to probe different regions of the sample. Measurements were

analyzed using *musrfit* [56]. The magnetically ordered volume fraction of the (111)LNO was calculated using

$$F_M(T) = \left(1 - \frac{A(T)}{A_{above}}\right) \frac{1}{F_{stop}}, \quad (3)$$

where A_{above} is the asymmetry above the suspected magnetic transition temperature, and F_{stop} represents the fraction of the muons stopping within the film.

Zero-field measurements were taken on the same samples after a degaussing of the magnet, and the muon spin-polarization asymmetry was fit to a combination of a rapid decay with a Gaussian lineshape and a slower stretched exponential function, as described in the main text.

Here, we note that there are significant differences between bulk μ SR measurements, which implant very high-energy (4 MeV) muons, and LE- μ SR, which generally utilizes muons with kinetic energies between 1 keV and 30 keV. Because of the lower muon velocity in LE- μ SR, there is a much wider spread in the muon arrival times, so that oscillations of a muon that are significantly faster than the width of the distribution of muon implantation times will not appear in the data [57,58]. As discussed in the main text, LE- μ SR therefore has a much lower inherent time resolution than measurements utilizing 4 MeV muons.

One associated limitation of the technique is the requirement that measurements be performed in a weak applied field in order to observe asymmetry oscillations. Relying on the internal magnetic order of the system, as in Ref. [59], will yield no useful signal. Instead, the fraction of muons stopping in a magnetically ordered region of the film is probed inversely using measurements in a weak applied transverse magnetic field which induced precession at a detectable frequency. Muons stopped in a magnetically ordered region do not contribute to the asymmetry signal, such that normalizing to a high-temperature nonmagnetic background allows F_M to be calculated. In this way, it has been robustly demonstrated that weak transverse-field LE- μ SR may be used to track F_M [60]. Further, zero-field LE- μ SR is demonstrated to be sensitive to changes in magnetic order even in very thin films, although the information can be more challenging to extract [61].

E. Scanning Transmission Electron Microscopy

Scanning transmission electron microscopy (STEM) experiments were performed at the Material Measurement Laboratory at the National Institute of Standards and Technology using a Thermo Fisher Titan 80 to 300 keV (S)TEM instrument operating with a primary beam energy of 300 keV. High-resolution annular dark field (ADF) images were acquired using a Fischione high-angle annular dark field (HAADF) detector with a convergence semi-angle of 24 mrad and an inner collection semi-angle of approximately 60 mrad. To obtain a high signal-to-noise image with minimal specimen drift, 12 to 15 scans taken with a dwell time of 1 μ s per pixel were acquired, aligned via cross-correlation, and averaged to form a single image.

The strain maps were created by scanning nanobeam electron diffraction measurements. Diffraction patterns were collected at each point in the scan using a Merlin Medipix

3RX from Quantum Detectors. The acquisition time for each pattern was 2 ms and the pixel size of the scan was 1 nm. To extract lattice parameters and strain maps, the Fourier transform of the logarithm of the diffracted spots was calculated, following the exit wave power cepstrum (EWPC) method as described in Ref. [62].

F. Density Functional Theory calculations

The DFT+ U calculations on $(\text{LaNiO}_3)_N/(\text{LaAlO}_3)_M(111)$ were carried out with the Vienna *ab initio* Simulation Package (VASP) [63] code using the projector augmented wave method [64]. The generalized gradient approximation (GGA) of Perdew, Burke, and Ernzerhof has been applied for the exchange-correlation functional with an on-site Coulomb repulsion parameter considered within the GGA+ U approach to take into account the static local electronic correlations with $U = 5$ eV and Hund's exchange parameter of $J = 0.7$ eV (Ni 3d) and $U = 8$ eV (La 4f). We used the approach of Dudarev *et al.* [65], which considers $U_{eff} = U - J$. The lateral lattice constant is fixed to $a_{\text{LAO}} = 3.79$ Å, corresponding to an epitaxial growth on an LAO(111) substrate used in the experiments. The simulation cell of the perovskite-derived SL [see Fig. 5(a)] contains 120 atoms (24 La, 72 oxygens, eight Al, and 16 Ni cations). The calculations were performed using a Γ centered k -point mesh of $4 \times 8 \times 2$ and the plane-wave cutoff energy was fixed to 500 eV. The lattice parameter c and the atomic positions were optimized until the Hellman-Feynman forces were less than 10 meV/Å. Due to the large supercell size used for DFT calculations, spin-orbit interactions were not considered.

ACKNOWLEDGMENTS

The research was supported by the U.S. Department of Energy, Director, Office of Science, Office of Basic Energy Sciences, Division of Materials Sciences and Engineering under Contract No. DESC0008505. A portion of this research used resources at the MAGREF beamline at the Spallation Neutron Source, a DOE Office of Science User Facility operated by the Oak Ridge National Laboratory. Access to CANDOR was provided by the Center for High Resolution Neutron Scattering, a partnership between the National Institute of Standards and Technology and the National Science Foundation under Agreement No. DMR-2010792. Part of this work was performed at the Stanford Nano Shared Facilities (SNSF), supported by the National Science Foundation under Award No. EECs-1542152. This work is based on experiments performed at the Swiss Muon Source μ S, Paul Scherrer Institute, Villigen, Switzerland. This material is based upon work supported by the National Science Foundation Graduate Research Fellowship Grant No. DGE-1656518. O.K. and R.P. acknowledge computational time at the Leibniz Rechenzentrum Garching, project pr87ro. Certain trade names and commercial equipment and instruments are identified to specify adequately the experimental procedure. Such identification does not imply recommendation or endorsement by the National Institute of Standards and Technology, nor does it imply that the equipment identified are necessarily the best for the purpose.

- [1] P. Wadley, B. Howells, J. Železný, C. Andrews, V. Hills, R. P. Campion, V. Novák, K. Olejník, F. Maccherozzi, S. Dhesi *et al.*, Electrical switching of an antiferromagnet, *Science* **351**, 587 (2016).
- [2] H. Tsai, T. Higo, K. Kondou, T. Nomoto, A. Sakai, A. Kobayashi, T. Nakano, K. Yakushiji, R. Arita, S. Miwa *et al.*, Electrical manipulation of a topological antiferromagnetic state, *Nature (London)* **580**, 608 (2020).
- [3] Y. Takeuchi, Y. Yamane, J.-Y. Yoon, R. Itoh, B. Jinnai, S. Kanai, J. Ieda, S. Fukami, and H. Ohno, Chiral-spin rotation of non-collinear antiferromagnet by spin-orbit torque, *Nat. Mater.* **20**, 1364 (2021).
- [4] T. Higo, K. Kondou, T. Nomoto, M. Shiga, S. Sakamoto, X. Chen, D. Nishio-Hamane, R. Arita, Y. Otani, S. Miwa *et al.*, Perpendicular full switching of chiral antiferromagnetic order by current, *Nature (London)* **607**, 474 (2022).
- [5] P. Vaidya, S. A. Morley, J. van Tol, Y. Liu, R. Cheng, A. Brataas, D. Lederman, and E. Del Barco, Subterahertz spin pumping from an insulating antiferromagnet, *Science* **368**, 160 (2020).
- [6] J. Han, P. Zhang, Z. Bi, Y. Fan, T. S. Safi, J. Xiang, J. Finley, L. Fu, R. Cheng, and L. Liu, Birefringence-like spin transport via linearly polarized antiferromagnetic magnons, *Nat. Nanotechnol.* **15**, 563 (2020).
- [7] J. Li, C. B. Wilson, R. Cheng, M. Lohmann, M. Kavand, W. Yuan, M. Aldosary, N. Agladze, P. Wei, M. S. Sherwin *et al.*, Spin current from sub-terahertz-generated antiferromagnetic magnons, *Nature (London)* **578**, 70 (2020).
- [8] Y. Wang, D. Zhu, Y. Yang, K. Lee, R. Mishra, G. Go, S.-H. Oh, D.-H. Kim, K. Cai, E. Liu *et al.*, Magnetization switching by magnon-mediated spin torque through an antiferromagnetic insulator, *Science* **366**, 1125 (2019).
- [9] T. Berlijn, P. C. Snijders, O. Delaire, H.-D. Zhou, T. A. Maier, H.-B. Cao, S.-X. Chi, M. Matsuda, Y. Wang, M. R. Koehler, P. R. C. Kent, and H. H. Weitering, Itinerant antiferromagnetism in RuO₂, *Phys. Rev. Lett.* **118**, 077201 (2017).
- [10] A. C. Komarek, S. V. Streltsov, M. Isobe, T. Möller, M. Hoelzel, A. Senyshyn, D. Trots, M. T. Fernández-Díaz, T. Hansen, H. Gotou, T. Yagi, Y. Ueda, V. I. Anisimov, M. Grüninger, D. I. Khomskii, and M. Braden, CaCrO₃: An anomalous antiferromagnetic metallic oxide, *Phys. Rev. Lett.* **101**, 167204 (2008).
- [11] P. A. Bhobe, A. Chainani, M. Taguchi, R. Eguchi, M. Matsunami, T. Ohtsuki, K. Ishizaka, M. Okawa, M. Oura, Y. Senba, H. Ohashi, M. Isobe, Y. Ueda, and S. Shin, Electronic structure of an antiferromagnetic metal: CaCrO₃, *Phys. Rev. B* **83**, 165132 (2011).
- [12] S. Catalano, M. Gibert, J. Fowlie, J. Íñiguez, J.-M. Triscone, and J. Kreisel, Rare-earth nickelates RNiO₃: Thin films and heterostructures, *Rep. Prog. Phys.* **81**, 046501 (2018).
- [13] Q. Song, S. Doyle, G. A. Pan, I. El Baggari, D. Ferenc Segedin, D. Córdova Carrizales, J. Nordlander, C. Tzschaschel, J. R. Ehrets, Z. Hasan, H. El-Sherif, J. Krishna, C. Hanson, H. LaBollita, A. Bostwick, C. Jozwiak, E. Rotenberg, S.-Y. Xu, A. Lanzara, A. T. N'Diaye *et al.*, Antiferromagnetic metal phase in an electron-doped rare-earth nickelate, *Nat. Phys.* **19**, 522 (2023).
- [14] J. Son, P. Moetakef, J. M. Lebeau, D. Ouellette, L. Balents, S. J. Allen, and S. Stemmer, Low-dimensional mott material: Transport in ultrathin epitaxial LaNiO₃ films, *Appl. Phys. Lett.* **96**, 062114 (2010).
- [15] H. K. Yoo, S. I. Hyun, L. Moreschini, H.-D. Kim, Y. J. Chang, C. H. Sohn, D. W. Jeong, S. Sinn, Y. S. Kim, A. Bostwick *et al.*, Latent instabilities in metallic LaNiO₃ films by strain control of fermi-surface topology, *Sci. Rep.* **5** (2015).
- [16] E. J. Moon, B. A. Gray, M. Kareev, J. Liu, S. G. Altendorf, F. Strigari, L. H. Tjeng, J. W. Freeland, and J. Chakhalian, Strain-dependent transport properties of the ultra-thin correlated metal, LaNiO₃, *New J. Phys.* **13**, 073037 (2011).
- [17] J. Fowlie, M. Gibert, G. Tieri, A. Gloter, J. Iniguez, A. Filippetti, S. Catalano, S. Gariglio, A. Schober, M. Guennou *et al.*, Conductivity and local structure of LaNiO₃ thin films, *Adv. Mater.* **29**, 1605197 (2017).
- [18] J. Fowlie, C. Lichtensteiger, M. Gibert, H. Meley, P. Willmott, and J.-M. Triscone, Thickness-dependent perovskite octahedral distortions at heterointerfaces, *Nano Lett.* **19**, 4188 (2019).
- [19] R. Scherwitzl, S. Gariglio, M. Gabay, P. Zubko, M. Gibert, and J.-M. Triscone, Metal-insulator transition in ultrathin LaNiO₃ films, *Phys. Rev. Lett.* **106**, 246403 (2011).
- [20] A. X. Gray, A. Janotti, J. Son, J. M. Lebeau, S. Ueda, Y. Yamashita, K. Kobayashi, A. M. Kaiser, R. Sutarto, H. Wadati *et al.*, Insulating state of ultrathin epitaxial LaNiO₃ thin films detected by hard x-ray photoemission, *Phys. Rev. B* **84**, 075104 (2011).
- [21] E. Sakai, M. Tamamitsu, K. Yoshimatsu, S. Okamoto, K. Horiba, M. Oshima, and H. Kumigashira, Gradual localization of Ni-3d states in LaNiO₃ ultrathin films induced by dimensional crossover, *Phys. Rev. B* **87**, 075132 (2013).
- [22] C. Liu, V. F. C. Humbert, T. M. Bretz-Sullivan, G. Wang, D. Hong, F. Wrobel, J. Zhang, J. D. Hoffman, J. E. Pearson, J. S. Jiang, C. Chang, A. Suslov, N. Mason, M. R. Norman, and A. Bhattacharya, Observation of an antiferromagnetic quantum critical point in high-purity LaNiO₃, *Nat. Commun.* **11**, 1402 (2020).
- [23] A. Blanca-Romero and R. Pentcheva, Confinement-induced metal-to-insulator transition in strained LaNiO₃/LaAlO₃ superlattices, *Phys. Rev. B* **84**, 195450 (2011).
- [24] M. Verma and R. Pentcheva, Tuning the carrier localization, magnetic and thermoelectric properties of ultrathin (LaNiO_{3-δ})₁/(LaAlO₃)₁(001) superlattices by oxygen vacancies, *Phys. Rev. Res.* **6**, 013189 (2024).
- [25] T. Asaba, Z. Xiang, T. H. Kim, M. S. Rzechowski, C. B. Eom, and L. Li, Unconventional ferromagnetism in epitaxial (111) LaNiO₃, *Phys. Rev. B* **98**, 121105 (2018).
- [26] M. M. Kane, A. Vailionis, L. J. Riddiford, A. Mehta, A. T. N'Diaye, C. Klewe, P. Shafer, E. Arenholz, and Y. Suzuki, Emergent long-range magnetic order in ultrathin (111)-oriented LaNiO₃ films, *npj Quantum Mater.* **6**, 44 (2021).
- [27] D. Doennig, W. E. Pickett, and R. Pentcheva, Confinement-driven transitions between topological and Mott phases in (LaNiO₃)_N/(LaAlO₃)_M(111) superlattices, *Phys. Rev. B* **89**, 121110(R) (2014).
- [28] H. Chen, Q. Niu, and A. H. MacDonald, Anomalous hall effect arising from noncollinear antiferromagnetism, *Phys. Rev. Lett.* **112**, 017205 (2014).
- [29] N. J. Ghimire, A. S. Botana, J. S. Jiang, J. Zhang, Y.-S. Chen, and J. F. Mitchell, Large anomalous Hall effect in the chiral-lattice antiferromagnet CoNb₃S₆, *Nat. Commun.* **9**, 3280 (2018).
- [30] See Supplemental Material at <http://link.aps.org/supplemental/10.1103/PhysRevMaterials.8.124406> for additional transport

- measurements, additional analysis of the polarized neutron reflectometry, additional analysis of the muon spin relaxation measurements, and x-ray absorption spectroscopy measurements.
- [31] M. Hara, J. Sakurai, S. Akamaru, K. Watanabe, K. Nishimura, K. Mori, and M. Matsuyama, Magnetic properties of palladium and palladium; Platinum alloy of various hydrogen content, *Mater. Trans.* **47**, 2373 (2006).
- [32] A. Hernando, B. Sampedro, M. A. Garcia, P. Marin, G. Rivero, P. Crespo, and J. M. Gonzalez, Palladium: A localised paramagnetism, [arXiv:cond-mat/0605496](https://arxiv.org/abs/cond-mat/0605496).
- [33] W. Gerhardt, F. Razavi, J. S. Schilling, D. Hüser, and J. A. Mydosh, Pressure dependence of the magnetic susceptibility of pure Pd to 3.7 GPa from 1.3 to 300 K, *Phys. Rev. B* **24**, 6744 (1981).
- [34] H. Guo, Z. W. Li, L. Zhao, Z. Hu, C. F. Chang, C.-Y. Kuo, W. Schmidt, A. Piovano, T. W. Pi, O. Sobolev *et al.*, Antiferromagnetic correlations in the metallic strongly correlated transition metal oxide LaNiO_3 , *Nat. Commun.* **9**, 43 (2018).
- [35] R. D. Sánchez, M. T. Causa, A. Caneiro, A. Butera, M. Vallet-Regí, M. J. Sayaguós, J. González-Calbet, F. García-Sanz, and J. Rivas, Metal-insulator transition in oxygen-deficient LaNiO_{3-x} perovskites, *Phys. Rev. B* **54**, 16574 (1996).
- [36] B.-X. Wang, S. Rosenkranz, X. Rui, J. Zhang, F. Ye, H. Zheng, R. F. Klie, J. F. Mitchell, and D. Phelan, Antiferromagnetic defect structure in $\text{LaNiO}_{3-\delta}$ single crystals, *Phys. Rev. Mater.* **2**, 064404 (2018).
- [37] Y. Shin and J. M. Rondinelli, Magnetic structure of oxygen-deficient perovskite nickelates with ordered vacancies, *Phys. Rev. Res.* **4**, L022069 (2022).
- [38] X. Liao, V. Singh, and H. Park, Oxygen vacancy induced site-selective Mott transition in LaNiO_3 , *Phys. Rev. B* **103**, 085110 (2021).
- [39] J. Zhang, H. Zheng, Y. Ren, and J. Mitchell, High-pressure floating-zone growth of perovskite nickelate LaNiO_3 single crystals, *Cryst. Growth Des.* **17**, 2730 (2017).
- [40] D. Meyers, S. Middey, M. Kareev, M. van Veenendaal, E. J. Moon, B. A. Gray, J. Liu, J. W. Freeland, and J. Chakhalian, Strain-modulated Mott transition in EuNiO_3 ultrathin films, *Phys. Rev. B* **88**, 075116 (2013).
- [41] S. Catalano, M. Gibert, V. Bisogni, O. E. Peil, F. He, R. Sutarto, M. Viret, P. Zubko, R. Scherwitzl, A. Georges *et al.*, Electronic transitions in strained SmNiO_3 thin films, *APL Mater.* **2**, 116110 (2014).
- [42] J. DeNatale and P. Kobrin, Lattice distortion effects on electrical switching in epitaxial thin film NdNiO_3 , *J. Mater. Res.* **10**, 2992 (1995).
- [43] L. Feigl, B. Schultz, S. Ohya, D. Ouellette, A. Kozhanov, and C. Palmstrøm, Structural and transport properties of epitaxial PrNiO_3 thin films grown by molecular beam epitaxy, *J. Cryst. Growth* **366**, 51 (2013).
- [44] M. Gibert, M. Viret, P. Zubko, N. Jaouen, J.-M. Tonnerre, A. Torres-Pardo, S. Catalano, A. Gloter, O. Stóphan, and J.-M. Triscone, Interlayer coupling through a dimensionality-induced magnetic state, *Nat. Commun.* **7**, 11227 (2016).
- [45] G. Zhou, C. Song, Y. Bai, Z. Quan, F. Jiang, W. Liu, Y. Xu, S. S. Dhesi, and X. Xu, Robust interfacial exchange bias and metal-insulator transition influenced by the LaNiO_3 layer thickness in $\text{La}_{0.7}\text{Sr}_{0.33}\text{MnO}_3/\text{LaNiO}_3$ superlattices, *ACS Appl. Mater. Interfaces* **9**, 3156 (2017).
- [46] G. Zhou, Z. Yan, Y. Bai, J. Zang, Z. Quan, S. Qi, and X. Xu, Exchange bias effect and orbital reconstruction in (001)-oriented $\text{LaMnO}_3/\text{LaNiO}_3$ superlattices, *ACS Appl. Mater. Interfaces* **9**, 39855 (2017).
- [47] G. Zhou, H. Ji, J. Zhang, Y. Bai, Z. Quan, and X. Xu, The antiferromagnetic state in ultrathin LaNiO_3 layer supported by long-range exchange bias in $\text{LaNiO}_3/\text{SrTiO}_3/\text{La}_{0.7}\text{Sr}_{0.3}\text{MnO}_3$ superlattices, *J. Mater. Chem. C* **6**, 582 (2018).
- [48] A. V. Boris, Y. Matiks, E. Benckiser, A. Frano, P. Popovich, V. Hinkov, P. Wochner, M. Castro-Colin, E. Detemple, V. K. Malik, C. Bernhard, T. Prokscha, A. Suter, Z. Salman, E. Morenzoni, G. Cristiani, H.-U. Habermeier, and B. Keimer, Dimensionality control of electronic phase transitions in nickel-oxide superlattices, *Science* **332**, 937 (2011).
- [49] J. D. Hoffman, B. J. Kirby, J. Kwon, G. Fabbri, D. Meyers, J. W. Freeland, I. Martin, O. G. Heinonen, P. Steadman, H. Zhou, C. M. Schlepütz, M. P. M. Dean, S. G. E. te Velthuis, J.-M. Zuo, and A. Bhattacharya, Oscillatory noncollinear magnetism induced by interfacial charge transfer in superlattices composed of metallic oxides, *Phys. Rev. X* **6**, 041038 (2016).
- [50] X. Q. Xu, J. L. Peng, Z. Y. Li, H. L. Ju, and R. L. Greene, Resistivity, thermopower, and susceptibility of $R\text{NiO}_3$ ($R = \text{La}, \text{Pr}$), *Phys. Rev. B* **48**, 1112 (1993).
- [51] H. Seim, H. Mölså, M. Nieminen, H. Fjellvåg, and L. Niinistö, Deposition of LaNiO_3 thin films in an atomic layer epitaxy reactor, *J. Mater. Chem.* **7**, 449 (1997).
- [52] B. J. Kirby, P. A. Kienzle, B. B. Maranville, N. F. Berk, J. Krycka, F. Heinrich, and C. F. Majkrzak, Phase-sensitive specular neutron reflectometry for imaging the nanometer scale composition depth profile of thin-film materials, *Current Opinion Coll. & Inter. Sci.* **17**, 44 (2012).
- [53] B. Maranville, W. Ratcliff II, and P. Kienzle, reductus: A stateless python data reduction service with a browser front end, *J. Appl. Crystallogr.* **51**, 1500 (2018).
- [54] E. Morenzoni, H. Glückler, T. Prokscha, R. Khasanov, H. Luetkens, M. Birke, E. Forgan, C. Niedermayer, and M. Pleines, Implantation studies of keV positive muons in thin metallic layers, *Nucl. Instrum. Methods Phys. Res., Sect. B* **192**, 254 (2002).
- [55] T. Prokscha, E. Morenzoni, K. Deiters, F. Foroughi, D. George, R. Kobler, A. Suter, and V. Vrankovic, The new $\mu\text{E}4$ beam at PSI: A hybrid-type large acceptance channel for the generation of a high intensity surface-muon beam, *Nucl. Instrum. Methods Phys. Res., Sect. A* **595**, 317 (2008).
- [56] A. Suter and B. Wojek, Musrfit: A free platform-independent framework for μSR data analysis, *Phys. Procedia* **30**, 69 (2012).
- [57] E. Morenzoni, H. Glückler, T. Prokscha, H. Weber, E. Forgan, T. Jackson, H. Luetkens, C. Niedermayer, M. Pleines, M. Birke *et al.*, Low-energy μSR at PSI: Present and future, *Phys. B: Condens. Matter* **289-290**, 653 (2000).
- [58] A. Suter, M. M. Martins, X. Ni, T. Prokscha, and Z. Salman, Low energy measurements in low-energy μSR , *J. Phys.: Conf. Ser.* **2462**, 012011 (2023).
- [59] H. Luetkens, M. Stingaciu, Y. G. Pashkevich, K. Conder, E. Pomjakushina, A. A. Gusev, K. V. Lamonova, P. Lemmens, and H.-H. Klauss, Microscopic evidence of spin state order and spin state phase separation in layered cobaltites $R\text{BaCo}_2\text{O}_{5.5}$ with $R = \text{Y}, \text{Tb}, \text{Dy}$, and Ho , *Phys. Rev. Lett.* **101**, 017601 (2008).

- [60] J. A. Krieger, C.-Z. Chang, M.-A. Husanu, D. Sostina, A. Ernst, M. M. Otrokov, T. Prokscha, T. Schmitt, A. Suter, M. G. Vergniory *et al.*, Spectroscopic perspective on the interplay between electronic and magnetic properties of magnetically doped topological insulators, *Phys. Rev. B* **96**, 184402 (2017).
- [61] J. Fowlie, M. Hadjimichael, M. M. Martins, D. Li, M. Osada, B. Y. Wang, K. Lee, Y. Lee, Z. Salman, T. Prokscha *et al.*, Intrinsic magnetism in superconducting infinite-layer nickelates, *Nat. Phys.* **18**, 1043 (2022).
- [62] E. Padgett, M. E. Holtz, P. Cueva, Y.-T. Shao, E. Langenberg, D. G. Schlom, and D. A. Muller, The exit-wave power-spectrum transform for scanning nanobeam electron diffraction: Robust strain mapping at subnanometer resolution and subpicometer precision, *Ultramicroscopy* **214**, 112994 (2020).
- [63] G. Kresse and J. Furthmüller, Efficient iterative schemes for *ab initio* total-energy calculations using a plane-wave basis set, *Phys. Rev. B* **54**, 11169 (1996).
- [64] G. Kresse and D. Joubert, From ultrasoft pseudopotentials to the projector augmented-wave method, *Phys. Rev. B* **59**, 1758 (1999).
- [65] S. L. Dudarev, G. A. Botton, S. Y. Savrasov, C. J. Humphreys, and A. P. Sutton, Electron-energy-loss spectra and the structural stability of nickel oxide: An LSDA+*U* study, *Phys. Rev. B* **57**, 1505 (1998).